ELSEVIER

Contents lists available at ScienceDirect

Carbohydrate Polymers

journal homepage: www.elsevier.com/locate/carbpol





Liquid uptake in porous cellulose sheets studied with UFI-NMR: Penetration, swelling and air displacement

R.J.K. Nicasy ^{a,1}, C. Waldner ^{c,d,2}, S.J.F. Erich ^{a,b,1,3}, O.C.G. Adan ^{a,b,3}, U. Hirn ^{c,d,2}, H. P. Huinink ^{a,*}

- ^a Eindhoven University of Technology, Applied Physics Department, P.O. Box 513, Eindhoven, 5600 MB, the Netherlands
- ^b Organization of Applied Scientific Research, TNO, P.O. Box 49, Delft, 2600 AA, the Netherlands
- ^c Institute of Bioproducts and Paper Technology, TU Graz, Inffeldgasse 23, 8010 Graz, Austria
- ^d CD Laboratory for Fiber Swelling and Paper Performance, Inffeldgasse 23, 8010 Graz, Austria

ARTICLE INFO

Keywords: NMR Cellulose Capillary uptake Swelling Paper Wetting

ABSTRACT

Liquid penetration in porous cellulosic materials is crucial in many technological fields. The complex geometry, small pore size, and often fast timescale of liquid uptake makes the process hard to capture. Effects such as swelling, vapor transport, film flow and water transport within cellulosic material makes transport deviate from well-known relations such as Lucas-Washburn and Darcy's Law. In this work it is demonstrated how Ultra-Fast Imaging NMR can be used to simultaneously monitor the liquid distribution and swelling during capillary uptake of water with a temporal- and spatial resolution of 10 ms and 14.5–18 µm respectively. The measurements show that in a cellulose fiber sheet, within the first 65 ms, liquid first penetrates the whole sheet before swelling takes place for another 30 s. Furthermore, it was observed that the liquid front traps 15 v% of air which is slowly replaced by water during the final stage of liquid uptake. Our method makes it possible to simultaneously quantify the concentration of all three phases (solid, liquid and air) within porous materials during processes exceeding 50 ms (5 times the temporal resolution). We hence believe that the proposed method should also be useful to study liquid penetration, or water diffusion, into other porous cellulosic materials like foams, membranes, nonwovens, textiles and films.

1. Introduction

Liquid uptake and swelling in biopolymer-based fiber sheets is crucial for multiple applications such as printing (Heard, Preston, Parsons, Cox, & Allen, 2004; Lamminmäki, Kettle, & Gane, 2011; Lundberg, Örtegren, Alfthan, & Ström, 2011), packaging (Han, Manolach, Denes, & Rowell, 2011; Kumar, Mukherjee, & Dutta, 2022; Kunam, Praveen, Akhila, & Gaikwad, 2022; Salem, Naithani, Jameel, Lucia, & Pal, 2022; Samyn, 2013), fiber-based microfluidic arrays, the textile industry (Parada, Vontobel, Rossi, Derome, & Carmeliet, 2017; Salam, Venditti, Pawlak, & El-Tahlawy, 2011; Tang, Wu, Chau, Kan, & Fan, 2015) and even the cleanup of spilled-oil (Zhang et al., 2022). The material offers

multiple advantages such as low cost, biodegradability and the easy manufacturing process (Tang, Kumar, Alavi, & Sandeep, 2012). In microfluidic devices such as bio-assays, fiber networks allow to operate without external pumps by using capillary forces to drive the liquids (Berli, See Claudio, Berli, Urteaga, & Berli, 2015). This makes fiber-based microfluidics highly valuable in low-income countries. To increase the efficiency of biopolymer-based applications, the biopolymers are often modified in order to improve the water absorbency, strength, and functionality (Salam et al., 2011). In packaging materials such as foams (Han et al., 2011) or biopolymer-based films the fibers are often made hydrophobic to strengthen the material and increase the water repellency (Cui et al., 2023; Han et al., 2011). The performance of these

^{*} Corresponding author at: Eindhoven Institute of Renewable Energy Systems, Eindhoven University of Technology, PO Box 513, Eindhoven 5600 MB, the Netherlands.

E-mail addresses: r.j.k.nicasy@tue.nl (R.J.K. Nicasy), bart.erich@tno.nl (S.J.F. Erich), olaf.adan@tno.nl (O.C.G. Adan), ulrich.hirn@tugraz.at (U. Hirn), h.p. huinink@tue.nl (H.P. Huinink).

¹ Transport in Permeable Media group, Department of Applied Physics, Eindhoven University of Technology, PO Box 513, Eindhoven 5600 MB, the Netherlands.

² Institute of Bioproducts and Paper Technology, Graz University of Technology, Inffeldgasse 23, 8010 Graz, Austria.

 $^{^{\}rm 3}\,$ TNO Materials Solution, High Tech Campus 25 Eindhoven, Netherlands.

applications relies on both the liquid flow through the sheet and their swelling behavior. Therefore, controlling and predicting the liquid flow and swelling are of great importance. Several studies are focused on the improvement of the swelling properties (Rohadi et al., 2021; Xu, Liu, Wang, Goff, & Zhong, 2020) and the dynamic wicking, (Parada et al., 2017) e.g. to improve the wear comfort of textiles (Tang et al., 2015) or the usability of edible films.

Another important example is paper, which is a complex system consisting of a network of wood pulp fibers (Alava & Niskanen, 2006). When liquid comes in contact with a cellulose fiber network, the liquid enters the pores between the fibers due to capillary forces. This process is mostly described by models such as Lucas-Washburn (Gong & Sinton, 2017; Patari & Mahapatra, 2020; Salminen, 1988; Waldner & Hirn, 2023) or Darcy's Law (Gong & Sinton, 2017; Kuijpers et al., 2018; Masoodi & Pillai, 2010). While both Laws show great potential to predict the fluid flow, deviations are commonly observed due to the complexity of the paper sheet (Patari & Mahapatra, 2020). Other processes effecting the imbibition are water transport through internal pores within the fibers (lumen) (Chang, Seo, Hong, Lee, & Kim, 2018; Salminen, 1988), vapor transport, evaporation, inertia effects (Ridgway, Gane, & Schoelkopf, 2002; Schoelkopf, Ridgway, Gane, Matthews, & Spielmann, 2000), a precursor front (De Azevedo, Alme, Engelsberg, Fossum, & Dommersnes, 2008) and swelling (Chang & Kim, 2020). The latter process deforms the porous structure during imbibition, resulting in deviations in the capillary uptake behavior. Efforts have been made to extend the existing models and incorporate processes such as swelling (Masoodi & Pillai, 2010) or liquid uptake by fibers (Chang et al., 2018). Due to the short timescale and small sizescale of the liquid penetration, it is hard to quantitatively capture and analyze these different processes in real time.

To improve our knowledge about various processes such as swelling and their influence on liquid imbibition in paper, foams, textiles and biopolymer-based films, experimental techniques that simultaneously measure swelling of the substrate and liquid uptake are of great importance. A number of experimental techniques exist, that are able to study moisture transport in thin fiber sheets such as optical transparency and infra-red spectroscopy (Murali, Venditti, Zeegers, & Darhuber, 2021; Venditti, Murali, & Darhuber, 2022; Wijburg, Wang, & Darhuber, 2023). These techniques are based on the attenuation of the radiation when passing through the paper sheets. They are well established to measure the lateral moisture distribution but are unable to evaluate the vertical moisture distribution. Other techniques such as Automatic Scanning Absorptometry (ASA) (Kuijpers et al., 2018), Ultrasonic Liquid Penetration (ULP) (Waldner & Hirn, 2020; Waldner, Mayrhofer, & Hirn, 2022) and Drop Adsorption (Waldner et al., 2022) are ideal tools to measure the total amount of liquid absorbed by a sheet. These methods meet the high temporal resolution required to measure water uptake but fail to provide spatial information. To gain information about the moisture distribution within the sheet, assumptions about the uptake process must be made. However, this becomes very difficult in a complex porous material, where the liquid uptake is still not clearly understood. Some new experimental methods try to cope with the complex nature of moisture uptake within paper. In a recent study by Ferreira et al., (Ferreira et al., 2023) it was shown that by using iron tracers, the researchers could identify multiple fluid fronts penetrating within a paper sheets. Furthermore, measurements of the iron content within the fibers, gave information about the way in which water penetrated within the cellulose fibers. While this method provides key information about the moisture uptake within paper sheets, the measurements were only performed on the lateral moisture uptake on timescales exceeding 1 s. Furthermore, the determination of the iron contents was very time consuming and could only be performed on fixed timescales. Therefore, a technique that is able to measure the through-thickness moisture distribution and swelling simultaneously with sufficient temporal and spatial resolution would be of great importance.

A promising candidate for measuring the moisture content in paper is

Nuclear Magnetic Resonance (NMR). NMR is a non-destructive measurement technique able to measure in-situ the through-thickness moisture profile in thin porous media and paper sheets by detecting the 1 H atoms (Blumich, 2000; Nicasy, Huinink, Erich, & Adan, 2022; Perrin, Waldner, Bossu, Chatterjee, & Hirn, 2022). 1 H atoms can be followed because of their spin ½ nucleus. Due to the spin ½ nucleus, the 1 H atoms have a magnetic moment that can be used to make them visible. During an NMR measurement, spins are aligned using a main magnetic field B_0 [T] while spatial information is obtained by using a magnetic field gradient with magnitude G [Tm $^{-1}$]. Due to these magnet fields, the spins will start to resonate with a specific frequency called the Larmor frequency. Using this frequency, a density profile of the spins can be extracted by performing a Fourier transform on the measured signal.

However, performing measurements on the uptake of water within paper is still challenging because of the timescales of some of the uptake processes (< 1 s) (Krainer, Smit, & Hirn, 2019), which are extremely fast for NMR imaging and the small thickness of paper (100 μm). Previously, we introduced an Ultra Fast Imaging (UFI) technique which allows to measure through-thickness moisture distributions in Nylon and PVDF membranes with a temporal- and spatial resolution of 10 ms and 14.5–18 µm (Nicasy, Huinink, Erich, & Adan, 2021). The technique uses a home build GARField NMR setup and acquisition system with a modified Ostroff-Waugh pulse sequence for multiple echo summations and the optimization of the penetration solution by the addition of a contrast agent. While this technique is still not fast enough to image processes such as inertia effects which are often described by the Bosanquet equation (Bosanquet, 1923), it offers great potential to study processes that exceed 50 ms such as capillary uptake, swelling, film flow and entrapment of air.

The aim of this work is to use the UFI method to study the complex penetration process of water into porous hydrophilic cellulosic materials by simultaneously monitoring the liquid distribution profile, material swelling, and displacement of entrapped air. It is believed that water uptake in hydrophilic cellulosic materials is governed by a capillary driven fluid front accompanied by swelling and that both processes can be decoupled. In the first part of this study, NMR-relaxation measurements on saturated paper samples are studied to identify which elements contribute to the UFI signal. In the second part, droplet uptake experiments are performed where the liquid distribution and swelling of a hydrophilic porous material will be analyzed. Finally, the acquired knowledge will be combined to come up with a model, describing the complex penetration process of water into the substrate.

2. Materials and methods

2.1. Substrate

In this work paper sheets were investigated, which were also used by Waldner et al., (Waldner et al., 2022; Waldner & Hirn, 2020; Waldner & Hirn, 2023). The sheets are from industrially produced uncoated printing paper (89.6 g/m²). The paper is composed of cellulose pulp (bleached eucalyptus kraft) and calcium carbonate filler particles (scalenohedral, precipitated calcium carbonate, filler content 21.25 %). The paper has a thickness of 120-130 µm and an average pore radius of 2.8 μm. The pore radii were measured by Waldner et al. by mercury intrusion porosometry, using an Autopore IV 9500 instrument from Micromeritics Instrument Corp. (Waldner et al., 2022; Waldner & Hirn, 2020; Waldner & Hirn, 2023). Fig. 1 shows Scanning Electron Microscopy images from the cross-section (a) and the surface (b) of the paper sample. The SEM images were taken on a FEI Quanta 600 using 10 kV. In the cross-section, fiber lumen can be seen, which are marked with red arrows. Because the sample was dry, the lumen were closed. However, it could be observed that the lumen at the top of the image extended to a couple of micrometers (blue line). The white parts in the image correspond to scalenohedral precipitated calcium carbonate filler particles.

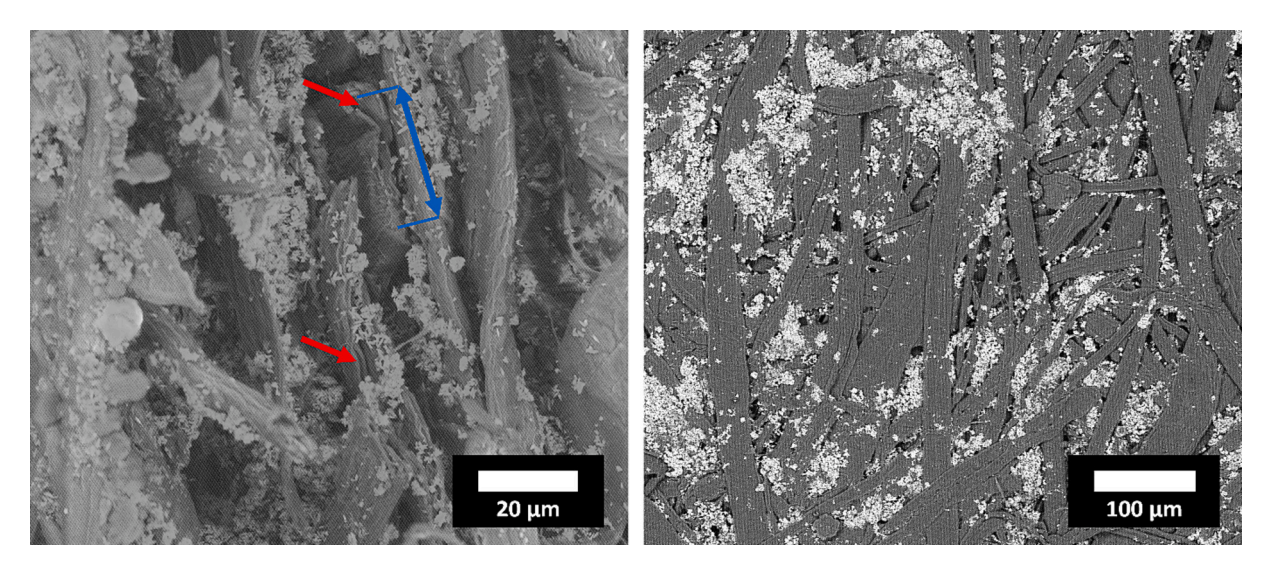


Fig. 1. scanning electron microscopy image of the cross-section and surface of the paper used. Red arrows are used to mark examples of fiber lumen while the blue arrow is used to mark the total length of the one lumen.

2.2. Test liquids

For the liquid uptake experiments, a ClariscanTM-water mixture was used, made as explained by Nicasy et al. (Nicasy, Huinink, Erich, Adan, & Tomozeiu, 2023). The mixture contains demineralized water of type I and 0.04 mol/l of ClariscanTM.

The viscosity and surface tension of the mixture were determined using an Anton Paar MCR302 rheometer (20 °C) and the pendant drop method (Bolden, Corder, Higdon, & Miller, 2015) to be 1.09 mPa.s and 67.3 mN.m $^{-1}$.Clariscan $^{\rm TM}$ is a gadolinium based contrast agent used in medical MRI (Merbach, Helm, & Toth, 2013). Clariscan $^{\rm TM}$ was provided by GE Healthcare AS in a water like solution with a concentration of 279.3 g/ml (0.5 M). The Clariscan $^{\rm TM}$ solution has a pH between 6.5 and 8, a density of 1.349 g/ml and a viscosity of 3.0 mPa.s. The reason for adding Clariscan $^{\rm TM}$ was to control the NMR relaxation times and improve the signal to noise ratio, allowing to measure profiles with a 10 ms temporal resolution.

2.3. Nuclear magnetic resonance measurements

NMR measurements were performed on a home-built GARField NMR setup with a home-built acquisition system (Glover, Aptaker, Bowler, Ciampi, & McDonald, 1999; Nicasy et al., 2022). The setup has a main magnetic field ($B_0[T]$) of 1.47 T and a static gradient (G [Tm $^{-1}$]) of 41.5 Tm $^{-1}$. The signal was recorded using a Radio Frequency (RF) coil which has a diameter of 4 mm. All data was analyzed using MATLAB version R2019a and fits were made using the fit function.

 T_2 relaxation time measurements were performed with an Ostroff-Waugh (OW) pulse sequence given by $\left(90_x^\circ - \tau - \left[90_y^\circ - \tau - \text{echo} - \tau\right]_n\right)$, where n represents the number of echoes that were measured (Nicasy et al., 2022; Ostroff & Waugh, 1966). The echo time ($t_e = 2\tau$) was set to 50 μ s for all experiments. To reduce the signal to noise ratio, the measurements were averaged 512 times. The time between two measurements (repetition time, t_r) was set to 50 ms for experiments with a Clariscan-water solution and to 500 ms for experiments with demineralized water. The pulse length for these experiments was set to 1 μ s.

 T_1 relaxation time measurements were performed with a saturation recovery sequence $\left[\left[\alpha_y^\circ - \tau_1\right]_m - \tau_2 - 90_x^\circ - \tau - 90_y^\circ - \text{echo}\right]_n$, where m=5 is the amount of saturation pulses, $\tau_1=200$ µs and $\alpha=70^\circ$ is the flip angle of the saturation pulse. The pulse sequence was repeated n=15 times, where for every repetition, τ_2 was varied between 100 µs and

35 ms to acquire echoes at 15 different time steps. (Markley, Horsley, & Klein, 1971; Nicasy et al., 2022). The pulse length for these experiments was set to 1 μ s.

The moisture profiles were measured using the UFI method which was described in earlier work (Nicasy et al., 2023). UFI uses an adaptation of the OW-sequence with two additional elements. First, a summation of multiple echoes, which ensures a rapid increase in the signal to noise ratio. Second, the optimization of the penetration medium by the addition of a contrast agent (Clariscan) to lower the T_1 relaxation time. The specific pulse sequence used in UFI is given by $90^{\circ}_{x} - \tau$ $\left[90_{y}^{\circ} - \tau - (\text{echo}) - \tau - 90_{-y}^{\circ} - \tau - (-\text{echo}) - \tau\right]_{N}$, where N = 16 represents the number of repetitions. The echo time $(t_e = 2\tau)$ was set to 50 μs with a window width of 40 μs. The repetition time (time between two pulsed experiments) was set to 10 ms. The system allows to record and store 80 profiles before it requires to transfer its data. This results in a 0.8 s measurement time (80 moisture profiles) followed by a 6-8 s deadtime. This approach allows to measure liquid distribution profiles with a temporal resolution of 10 ms and spatial resolution of 14.5 μm - 18 μm . The pulse length was set to 1 µs and kept constant throughout all experiment. The pulse length was set relatively short to achieve the maximum Field-Of-View which was around 400 μm.

2.4. Liquid uptake experiments

Liquid uptake experiments were performed on paper samples that were glued on top of a glass plate using double-sided sticky tape. Fig. 2 shows a schematic image of the experimental setup with the droplet insert and an example of a typical sample. Fig. 2 also shows a typical NMR measurement corresponding to the situation shown on the left, where the moisture content is measured as a function of the position. More moisture profiles during the imbibition in nylon- and pvdf-membranes can be found in earlier research (Nicasy et al., 2021; Nicasy et al., 2023). The sample was placed within a glass cylinder (inner diameter = 11 mm) which could be closed by a glass plate in order to slow down evaporation of the liquid. A light sensor was added that triggers the NMR measurement when a falling droplet was detected. The sensor was shielded by a Faraday cage to prevent noise emission towards the RF-coil.

The experimental procedures used within this study are depicted in Fig. 3. Experiment type I was used to measure the liquid profiles during fast and slow liquid uptake processes for a water-Clariscan solution while experiment type II was used to study the slow liquid uptake

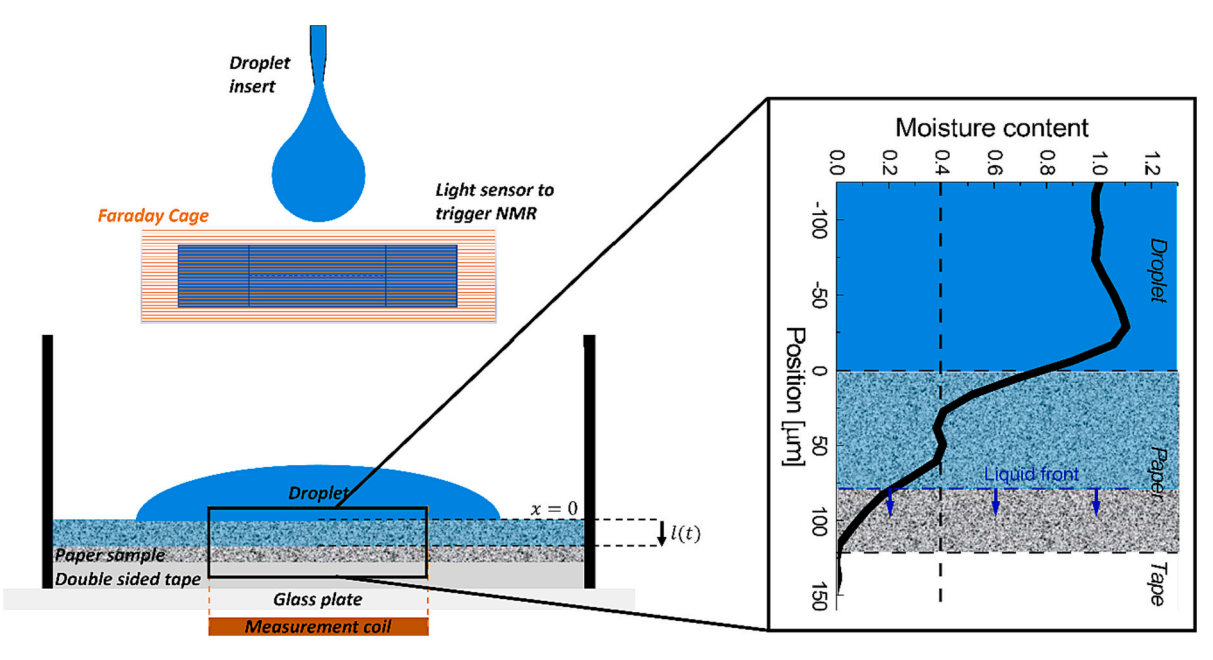


Fig. 2. Schematic picture of the measurement insert. Shown are the droplet insert, the light sensor to trigger the NMR, the sample with droplet and the RF coil to measure the signal.

processes for demineralized water.

Experiment type I starts by jetting a droplet (8–12 μ l) of the water-Clariscan solution on top of the paper sample, which triggers a light sensor that will start the NMR-pulse sequence. In all experiments the droplet radius (R), when in contant with the paper, is larger than 4 mm. This ensures that the droplet will not come in contact with the glass cylinder but is large enough to cover the whole measurement area, which is around 4 mm in diameter (RF-coil in Fig. 2). Liquid profiles are then measured using the UFI-pulse sequence. This is repeated 10 times and results in a 1 min window in which the fast processes are measured. To measure processes on longer timescales, the system is saturated by adding 5 more droplets and the compartment is closed with a glass plate to prevent evaporation. After closing the system, liquid profiles are measured by UFI every minute for a period of 150 min.

Experiment type II was performed to study the slower uptake processes in more detail by using demineralized water, where the T_2 relaxation time can provide extra valuable information. Because the procedure focusses on the slower processes, the system is directly saturated with 5 droplets of water and closed with a glass plate. After closing the system, the T_2 relaxation time and liquid profile are recorded by an OW sequence every 9 min for a time span of 4 h.

3. Results

3.1. NMR signal: the various hydrogen pools in wet paper

Water-containing cellulose fiber sheets are complex media, which consist of different hydrogen pools. To interpret UFI signal profiles, it is crucial to identify which hydrogen pools contribute to the measured signal. From the literature, it is known that within cellulose fiber networks such as paper different groups of hydrogen atoms can be discriminated, namely hydrogen from the fibers (cellulose, hemicellulose, lignin, ...), strongly bound water, ¹H atoms of fillers, sizing agents, liquid water inside the fiber lumen and liquid water between the fibers (Gezici-Koç, Erich, Huinink, van der Ven, & Adan, 2017; Rostom, Caré, & Denis Courtier-Murias., 2021). The main goal of this section is to identify which hydrogen pools will contribute to the signal as measured by UFI. Additionally, the measurements will provide more insight on the paper samples' morphology and composition, which can be used in later discussions.

To identify and characterize the NMR signal, T_2 measurements were performed on a saturated paper sheet containing various liquid solutions. As the measurements were performed in the presence of a constant magnetic gradient (41.5 T/m), the T_2 times reported within this study were effective T_2 times and not the true T_2 times. The samples were all saturated for at least 24 h to ensure that all transport processes were finished and that the samples were completely saturated. Fig. 4 shows the decay curves of demineralized water (black), demineralized water in paper (orange), a Clariscan solution (blue), a Clariscan solution in paper (green), and a paper sheet conditioned at a relative humidity of 100 % (yellow). The signal intensities of all experiments were rescaled always using the first echo of the free water signal intensity. For the measurements within paper, a multiexponential decay was observed which indicates the presence of various hydrogen pools. This was most visible in case the sample was conditioned at a relative humidity of 100 %, in which there was almost no liquid water. For a sample containing multiple hydrogen pools, the signal intensity obeys the following relation,

$$S \propto \sum_{i=1}^{\beta} \rho_i \left(1 - exp \left(-\frac{t_r}{T_{1i}} \right) \right) exp \left(-\frac{t_e}{T_{2i}} \right), \tag{1}$$

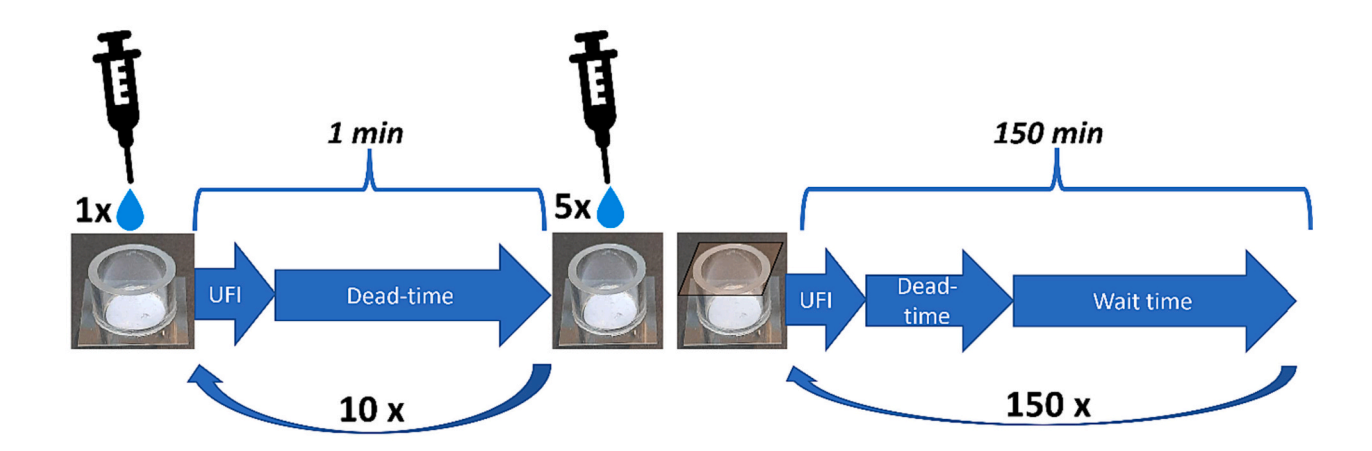
where the summation runs over all different pools of hydrogen nuclei ("i") within the porous system having a hydrogen density ρ_i and relaxation times T_{2i} [s] and T_{1i} [s]. Since the repetition time in all experiments was higher than $3T_1$ the influence of the T_1 factor is small and was neglected within the fitting procedure. Before discussing the determined T_2 relaxation times, a brief discussion about the T_2 relaxation time will be given which is needed to interpret the later determined values.

The T_2 -relaxation time is a complex parameter which depends on several environmental factors given by:

$$\frac{1}{T_2} = \frac{1}{T_{2bulk}} + \sigma \frac{A}{V} + \alpha D \gamma^2 G^2 t_e^2 + R_2 C.$$
 (2)

The terms on the right-hand side of the equation represent different relaxation mechanisms. The first term, $T_{2bulk}[ms]$, refers to relaxation in the bulk of the liquid phase, induced by dipolar interactions (Bloembergen-Purcell-Pound (BPP) theory (Bloembergen, Purcell, & Pound, 1948)). The second term, $\sigma A/V$, represents the surface relaxation of the porous media, which depends on the relaxivity of the material $\sigma[ms^{-1}]$ and the surface to volume ratio $A/V[m^{-1}]$ (Falzone & Keating, 2016;

Experiment Type I



Experiment Type II

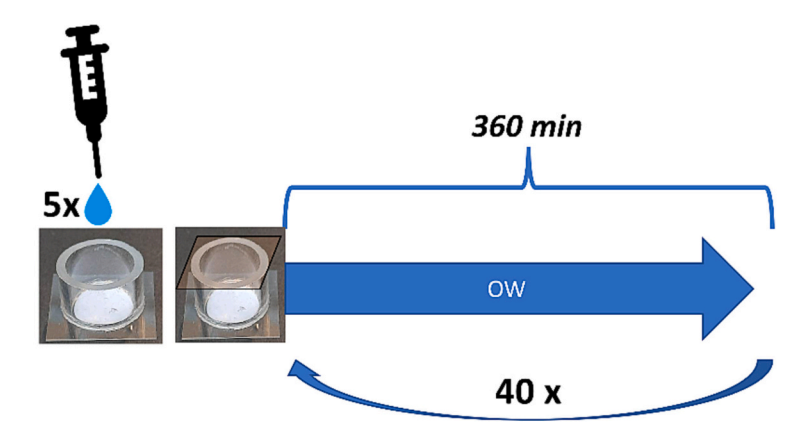


Fig. 3. a) Experiment type I to measure the liquid profiles during fast and slow liquid uptake of a Clariscan-water solution in paper. Part one of the measurement consists of a UFI measurement (0.8 s) followed by a 6-8 s dead-time which is repeated 10 times (total time = 1 min). Part two consists of the same UFI measurement (0.8 s) and dead time (6-8 s) but is now followed by a 1 min wait time. This part is repeated 150 times which results in a total time of 150 min. b) Experiment type II to study the liquid profiles and T_2 relaxation time for slow liquid uptake processes of demineralized water. The OW measurement takes 9 min and is repeated 40 times which results in a total measurement time of 360 min.

Müller-Petke, Dlugosch, Lehmann-Horn, & Ronczka, 2015). The third term, $aD\gamma^2G^2t_e^2$, represents the diffusion, which depends on the gyromagnetic ratio $\gamma[T^{-1}s^{-1}]$, effective diffusion $D[m^2s^{-1}]$, magnetic gradient $G[Tm^{-1}]$ and echo time $t_e[s]$ (Baukh, Huinink, Adan, Erich, & van der Ven, 2011; Hürlimann, 2001). Because the GARField NMR works with a constant gradient which cannot be turned off, this term will always contribute to the measured T_2 time. Therefore, the measured T_2 time is an effective T_2 time. The last term R_2C represents the relaxation of a contrast agent which depends on its concentration $C[m^{-3}]$ and its relaxation rate $R_2[s^{-1}m^3]$ (Jacques et al., 2010).

In the high-gradient GARField NMR, used in this study (Glover et al., 1999), the relaxation time for free water is mainly dominated by the diffusion term of Eq. (2) $((\alpha D \gamma^2 G^2 t_e^2)^{-1} \approx 11$ ms) (Baukh, Huinink, Adan, Erich, & van der L.G.J. Ven., 2012), and T_{2bulk} , which is around a few seconds, can be neglected.

When using Eq. (1), the decays of Fig. 4 can be fitted by setting $\beta=1$ in a free solution and $\beta=2$ within paper. The corresponding fits are shown as lines with similar colors.

Table 1 gives the fit parameters which we labeled long and short T_2

component respectively. It should be noted that in most NMR studies on paper samples, more hydrogen pools are discriminated such as bound water, cellulose, and other paper additives (Gezici-Koç et al., 2017; Rostom, Caré, & | Denis Courtier-Murias., 2021). The relaxation times of these components often lie between 0.1 ms and 2 ms. Due to the limited points within this time period and the rather low signal, these components could not be separated within our study and were therefore all combined within one component (short T_2 component).

When comparing the long T_2 component of demineralized water and demineralized water within a paper sheet, similar T_2 relaxation times were found ($T_2 \approx 12$ ms). In all cases the short component had a relaxation time around 50 μ s.

The relaxation time of the long T_2 component was close to its theoretical value of 11 ms as calculated from the diffusion term in Eq. (2). Therefore, it could be concluded that water within paper acted as free water. This behavior could be explained considering the large pore radius of the paper samples. When, after a pulse, hydrogen atoms were unable to diffuse to the fiber surfaces before a next refocusing pulse was given, surface relaxation, represented by the term $\sigma(A/V)$ in Eq. (2),

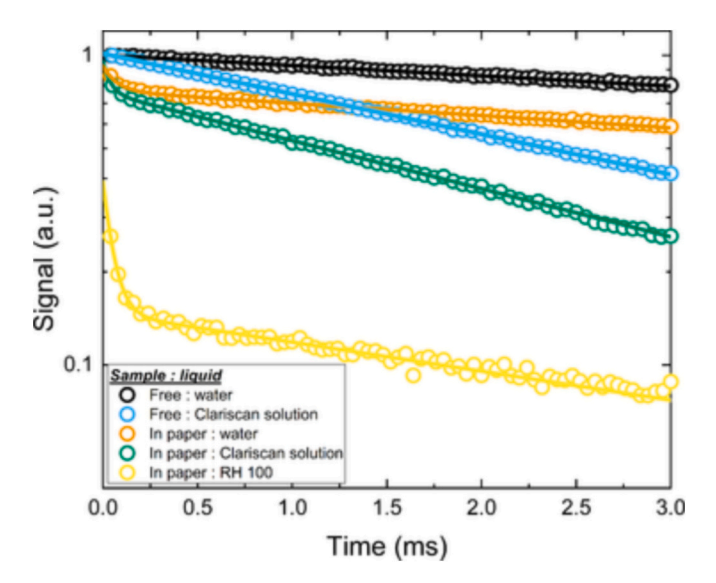


Fig. 4. T_2 signal decay measurements of demineralized water (black), a Clariscan reference solution (blue), demineralized water in a paper sample (orange) and Clariscan reference solution (green) in a paper sample. Also shown is a T_2 decay from a paper conditioned at a temperature of 25 $^{\circ}$ C with a relative humidity of 100 %.

Table 1 Short and long T_2 components for demineralized water, Clariscan solution, demineralized water within paper, Clariscan solution within paper and a paper conditioned at a temperature of 25 $^{\circ}$ C with a relative humidity of 100 %.

Sample	Short T_2 component		Long T_2 component	
	T ₂ [ms]	ρ_1	T_2 [ms]	ρ_2
Demineralized water	/	/	11.90	1.00
Clariscan solution	/	/	3.34	1.01
Demineralized water in paper	0.07	0.16	12.00	0.74
Clariscan solution in paper	0.05	0.20	2.90	0.80
Paper at RH100	0.05	0.24	4.64	0.17

would not occur. When using the self-diffusion coefficient of water at 22 °C, $D=2.1\times10^{-9} {\rm m^2 s^{-1}}$, and an echo time of 50 $\mu {\rm s}$, the diffusion length scale for free water could be calculated by $l=\sqrt{6Dt_e}=0.25~\mu {\rm m}$. Because the pores of the paper sample are 2.8 $\mu {\rm m}$, hence >10 times larger, the water behaved as free water within these experimental settings. The same could be said about water in completely swollen lumen (Topgaard & Söderman, 2001). From literature, it is known that lumen are typically one or more micrometers wide, therefore water within lumen will act as free water. As a result, the performed T_2 measurements could not discriminate water between fibers and water in lumen.

In the measurements that involve paper, a second T_2 component appeared. This was most visible in case the sample was conditioned at a relative humidity of 100 %, in which there was almost no liquid water. In all cases the short component had a relaxation time around 50 μ s, which corresponded to values found in literature for cellulose fibers and bound water, as reported by Rostom et al. (2020). Therefore, this component could mainly be attributed to the cellulose fibers but also other hydrogen groups such as bound water and hydrogen groups from fillers probably contributed to this signal. With a T_2 time of 50 μ s and a density of 20 v/v% the signal intensity of the small T_2 component was calculated to be 0.003. This was much lower than the actual noise level and therefore did not contribute to the UFI signal. Using this data, the relative fraction could provide information about the fiber content within the paper samples. In most cases, the fiber content occupied around 16–20 v% of a fully wet paper.

For a free Clariscan solution and a Clariscan solution within paper, similar decay curves were observed. For a Clariscan solution within

paper, again a short and long T_2 component were observed. The short component had a similar signal intensity as observed with free demineralized water and was around 16–20 %. The difference compared to free water was that the long T_2 components relaxation time was shortened from 12 to 3 ms due to the addition of a contrast agent.

Using these results, the following conclusions about the signal intensity within UFI could be made. The relaxation times of liquid within fiber lumen and between fibers were similar to those of free water. Therefore, signal from water within fiber lumen and in between fibers could not be discriminated and were both visible within the moisture profiles measured by UFI. The contribution of the signal of cellulose fibers, fillers and bound water, was too low to be measured by UFI. Therefore, the signal that was measured with UFI only came from liquid water between the fibers and within the fiber lumen. In a previous study, it was shown that by the addition of Clariscan, the relaxation times (T_1 and T_2) do not depend on the porous media and that the signal intensity is completely determined by the moisture content ρ (Nicasy et al., 2021). In the remainder of this study, all data will be represented by the moisture content instead of the signal intensity.

3.2. Water uptake in cellulose fiber networks: a three-phase process

The penetration of a Clariscan-water solution in paper was measured. This experiment revealed that water uptake in paper happened in 3 phases: a liquid front penetration phase, a swelling phase and liquid penetration on longer timescales. This section starts by showing the liquid distribution profiles, liquid front position, swelling and moisture content within the paper sheet. Next, the three phases will be introduced. Afterwards, every phase will be discussed in more detail in the subsequent subsections.

Measurements were performed using experiment type I. The moisture profiles for the penetration of a Clariscan solution in paper are shown in Fig. 5. Fig. 5a shows profiles between 0 and 75 ms, Fig. 5b shows profiles between 75 ms and 60 s, Fig. 5c shows profiles between 1 min and 180 min. In Fig. 5a-c, a green scale is used to identify the time at which the liquid profile was measured. In Fig. 5a and b, the paper is situated between 0 and 120 μ m with the droplet on top ($x < 0 \mu$ m) and the double-sided tape at the bottom ($x > 120 \mu m$). In Fig. 5c, the paper is increased in thickness and is situated between $-50 \ \text{and} \ 120 \ \mu\text{m}$ with the droplet on top ($x < -50 \,\mu\text{m}$) and the double-sided tape at the bottom (x> 120 μ m). More information about the 3D interpretation of these regions and profiles can be found in Fig. 2. Fig. 5a-c all represent another phase of the liquid uptake process. Fig. 5a, shows a liquid front penetrating inside the paper (arrow) while maintaining constant paper thickness. The increase in moisture content observed within the droplet during phase I was attributed to oscillations in the droplet. These oscillations lasted for approximately 50 ms and led to a movement of the hydrogen atoms during the pulse sequence. When the spatial displacement of the atoms was large compared to the spatial resolution of the setup, the misalignment of the spins during the refocusing pulses were large enough to significantly reduce the measured signal intensity. Fig. 5b illustrates the rapid increase in paper size (orange arrow) due to swelling and increase in moisture content (purple arrow). Finally, Fig. 5c shows how the moisture content within the paper kept increasing (arrow) even in the absence of further swelling.

Using the liquid profiles of Fig. 5, the liquid front position, paper swelling and moisture content within the paper sample could be extracted, which are shown in Fig. 6. The moisture content (Fig. 6a) was extracted from the profiles in Fig. 5 between 38 and 50 μm . Swelling (Fig. 6b), gives the thickness increase of the paper sheet in percent. The thickness of the paper sheet could be determined by the droplet-paper surface, which was extracted from the profiles of Fig. 5 at the position where the moisture content equals 0.8. The position of the liquid front (Fig. 6c) was extracted from the profiles of Fig. 5 by taking the position where the moisture content equals 0.2. The data showed how the moisture content rose in 3 different phases, all having their typical

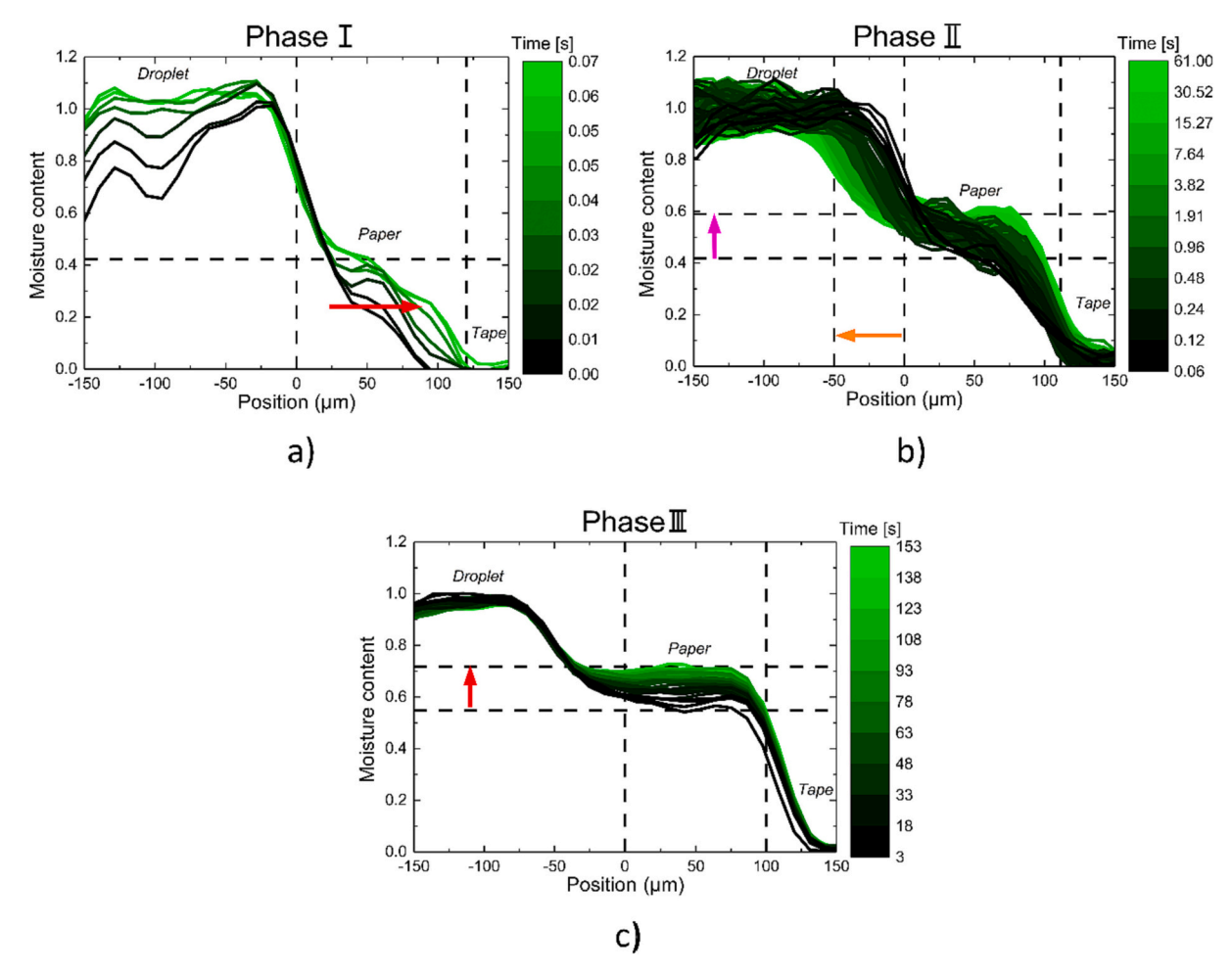


Fig. 5. Liquid profiles measured for the penetration of a water-Clariscan solution in paper sheets. Profiles are measured every 11.6 ms and are given for phase I (0 s < t < 0.07 s) (a), phase II (0.07 s < t < 61 s) (b) and phase III (61 s < t)(c). In every figure, a green colormap is used to specify the time of the corresponding liquid profile. Marked with lines are the interfaces and orange arrows are used to indicate the thickness increase that occurs in the paper during swelling.

timescale. Besides the changes in moisture content, it was observed that liquid front penetration mainly occurred in phase I, swelling mainly occurred in phase II and that both become negligible in phase III. The remainder of this section takes a closer look at every phase in order to explain the physical processes in the three phases.

3.2.1. Phase I: liquid penetration

After the droplet came in contact with the paper, liquid started to penetrate due to capillary forces. Fig. 5a shows how liquid penetrated with a front inside the paper. Fig. 7 shows the liquid front position as a function of \sqrt{t} for phase I. A linear relationship existed between the liquid front position and the \sqrt{t} , which could be related to Lucas Washburn and Darcy's law with a sharp front formalism where for both, the liquid front scaled with the square root of time (Kuijpers, Huinink, Tomozeiu, Erich, & Adan, 2017). After 65 ms the liquid front reached the end of the membrane, which marks the end of phase I. In this experiment, no swelling was observed during penetration. The moisture content after phase I was around 0.4 which ment that 60 v/v% of the area was filled with either air or fibers.

3.2.2. Phase II: swelling

After phase I (capillary uptake) was finished, the paper started to swell. Fig. 5b shows the moisture profiles during phase II. Swelling of the paper sheet became apparent from the movement of the droplet-paper interface, indicated by the horizontal arrow. The total time taken for the paper to reach maximum swelling was around 30 s. The swelling

could be investigated by tracking the droplet-paper interface over time. Fig. 8 shows both the liquid front positions (yellow) and swelling (black) for phase I and phase II in more detail. The data showed that during phase I, the liquid front position advanced while the swelling front stayed rather constant and that the opposite happened during phase II.

To analyze the swelling kinetics in more detail, a formula was adopted from literature (Botková, Šutý, Jablonský, Kucerkova, & Vrška, 2013; Jablonsky, Botková, Šutý, Šmatko, & Jozef, 2014; Letková, Letko, & Vrška, 2011) where the paper thickness increase (f[%]) is related to a rate constant (k (s⁻¹)) by:

$$f = f_{\text{max}} \left(1 - e^{-kt} \right), \tag{3}$$

where f_{max} stand for the maximum thickness increase of the paper. A fit of this model is shown in Fig. 8a (blue line) which gives a rate constant $k = 2.06s^{-1}$ and an $f_{max} = 45$ %.

Besides swelling, also the moisture content increased from 0.4 to 0.55 during phase II, see Fig. 5b. Fig. 8b shows the local moisture content within the paper between 38 and 50 μm (blue). To investigate in more depth the relation between the swelling of the paper and the observed moisture increase within the paper, the integrated moisture content between $-118~\mu m$ and $150~\mu m$ is also given in Fig. 8b (orange). This integrated moisture content, represents the total moisture content within the paper and part of the droplet that was replaced by paper after swelling, see Fig. 5b. At both ends, a margin was taken into account for the resolution of our setup. The figure illustrates how the integrated moisture content increased until 0.065 s, which corresponded to the

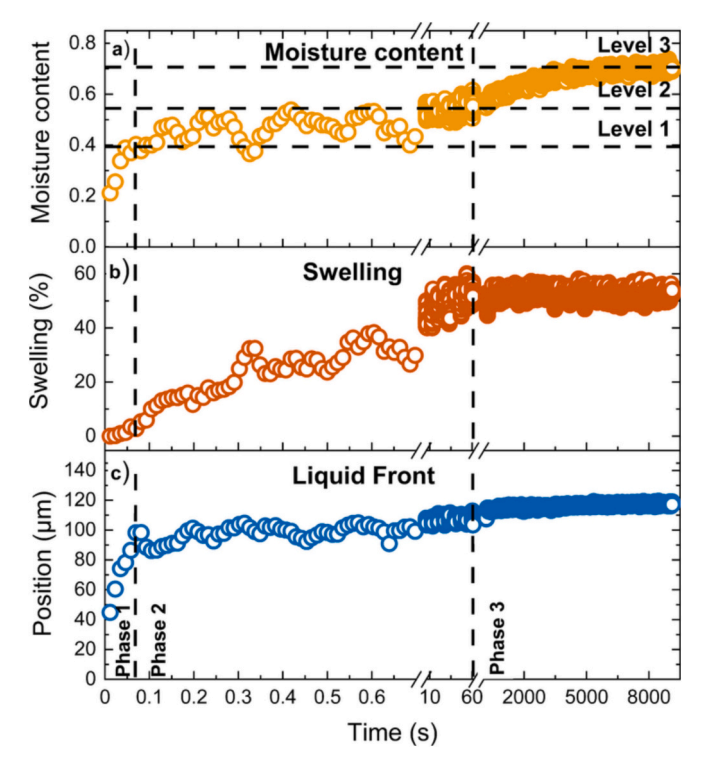


Fig. 6. a) Moisture content (yellow), b) swelling (orange) and c) liquid front position (blue) in a cellulose fiber sheet during liquid uptake of a water-Clariscan solution. Marked with lines are the different phases which all correspond to a typical moisture content level.

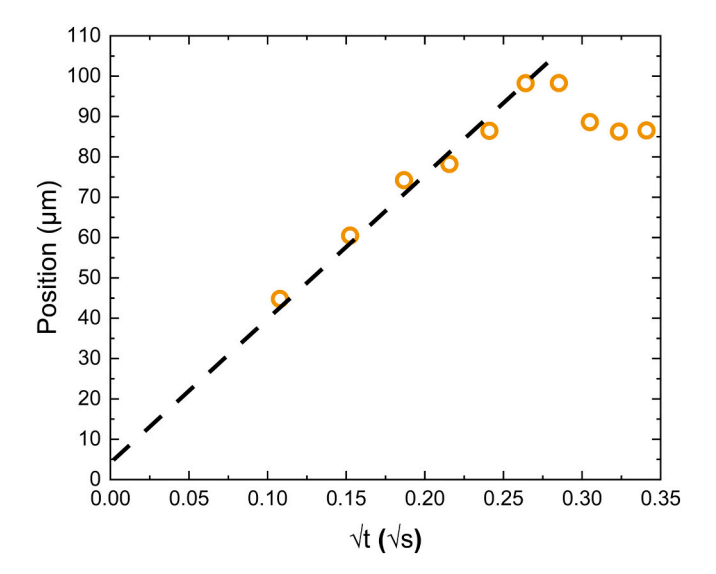


Fig. 7. Liquid front position as a function of \sqrt{t} for the penetration of a water-Clariscan solution in paper.

entering of the liquid front (phase I). However, during phase II it was observed that the total integrated moisture content between $-118~\mu m$ and $150~\mu m$ stayed constant. In Appendix A, it is proven that when the moisture content stays constant, the fiber content must remain constant. Therefore, the total fiber content within the paper stayed constant during swelling. When the fiber content within the paper stays constant and the paper thickness increases, the fiber concentration must go down. Therefore, swelling resulted in a redistribution of the fibers but leaves the total fiber content unchanged. A decrease in fiber concentration will in turn increase the porosity and increase the local moisture content.

Therefore, the increased moisture content in phase II could be linked to an increase in porosity when the paper swells. The end of phase II was marked by the end of swelling and by a constant moisture content of 0.55 within the paper.

After swelling, a third phase started, where the moisture content within paper continued to increase, see Fig. 5c. Fig. 6a shows how the moisture content increased from 0.55 to 0.72. An increase in the moisture content is accompanied by either a decrease in fiber content or a decrease in air content. Because no further changes in paper thickness

3.2.3. Phase III: release of trapped air results in a third moisture increase

were observed, see Fig. 5b, the fiber content had to remain constant. Therefore, there was still air within the paper sample which was gradually replaced by water and thereby increased the hydrogen content ρ measured by UFI. To confirm that the signal increase could not be attributed to changes in the T_1 and T_2 relaxation time, OW – and saturation recovery measurements were conducted during phase III for a Clariscan solution, the same solution used for the experiments. Fig. 2B shows the T_1 and T_2 relaxation time as a function of time during phase III. These measurements confirmed that both relaxation times were unchanged during phase III and could therefore not be responsible for the observed signal increase.

To investigate what happened during this last phase, OW experiments were performed to determine the T_2 of demineralized water on these later timescales. As explained in Section 2.3, the T_2 of demineralized water can provide valuable information about the environment of the hydrogen content, see Eq. (2). The measurements were performed according to experiment type II, see Fig. 3b. Fig. 9 shows the T_2 decays of demineralized water within a paper sheet during phase III. The data shows how the signal decay changed over time. From the signal decays, T_2 times were extracted which are shown in the indent of Fig. 9, where a line is used to mark the T_2 time of free water. The initial T_2 time of water was lower than the one of free water but increased to a value similar to free water. That water within paper acted similar to free water was already observed in Fig. 4. The period during which the T_2 changed, aligns closely with the time of the signal increase observed in Fig. 6a. Therefore, the mechanism responsible for the moisture increase was also responsible for the changes in the relaxation time.

It was already concluded that the release of trapped air was responsible for the increase in moisture content during phase III. The T_2 decay however can provide more information about the location of the trapped air. A closer look at Fig. 9 revealed that the change in decay time happened in the long component of the T_2 decay, which represents the majority of the signal. Because most of the water was between the fibers, the change in T_2 should be attributed to a phenomenon that took place between the fibers rather than within the fiber lumen. If the filling of the fiber lumen would be responsible for the signal increase, the relaxation behavior of the liquid between the fibers would be unchanged which was not observed. Therefore, it was concluded that the air was trapped between the fibers.

Since trapped air was responsible for the signal increase in phase III, the air content within the paper could be estimated by subtracting the liquid profiles in Fig. 5c from a fully saturated paper sample. Fig. 10 shows the air profiles calculated for phase III. The data shows that at the beginning of phase III, $14 \, v/v\%$ of the paper was filled with air, and that the air was homogeneously distributed throughout the sample. Over time the air escaped from the paper. Because of the experimental setup (Fig. 2) the air could only escape from the top of the paper. The movement of air to the top of the paper can be observed in the profiles of Fig. 10a marked with an arrow. From these profiles, the total air content within the paper could be calculated over time, which is shown in Fig. 10b.

4. Discussion

In this section, the previously introduced data are used to build up a

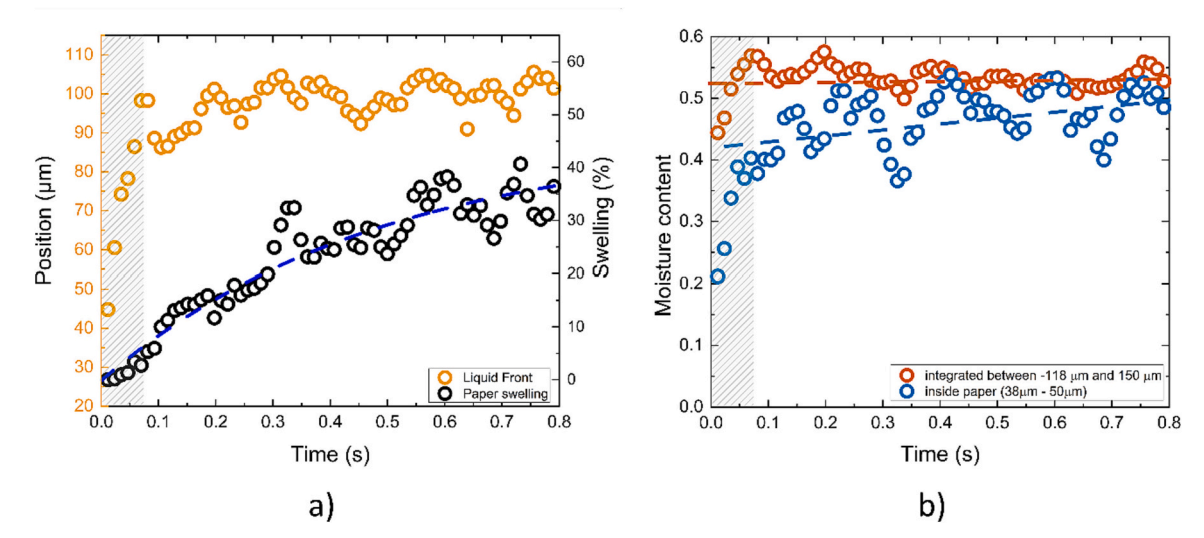


Fig. 8. a) Liquid front position (yellow) and swelling (black) for the penetration of a Clariscan-solution in paper. Phase I (penetration) and phase II (swelling) are marked by a different gray background. Shown with a blue line is a fit for the swelling kinetics. b) Moisture within the paper between 38 and 50 μ m (blue) and the integrated moisture content between -118 and 150 μ m (orange). The lines are drawn as guide for the eye.

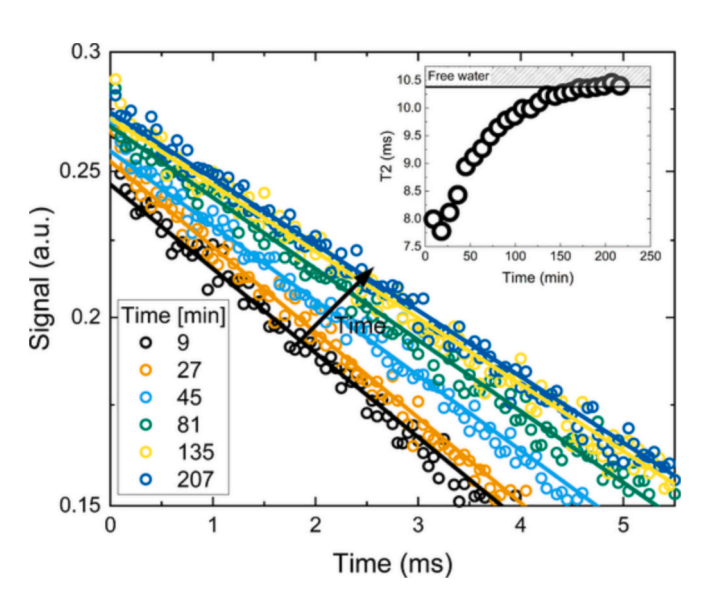


Fig. 9. OW-Signal decays during the penetration of water within a paper sheet between 30 and 60 μ m. Corresponding T_2 fits are shown with lines. The insert shows the extracted T_2 values as a function of time. The relaxation time of free demineralized water (10.3 ms) is also shown.

physical understanding about the water-filling mechanism inside a cellulose fiber network. Fig. 11 illustrates the relations between liquid front, swelling and moisture content in the network, with a green scale marking the time of each data point. Fig. 12 provides a schematic representation of the liquid filling mechanism. In this figure, the glass plate, network, and part of the droplet are shown. Gray is used for fibers, blue indicates liquid and white represents air. The orange circle marks the development of an air bubble within the paper sample.

During phase I, Fig. 12a, the liquid front (red line) enters the paper because of capillary forces. Capillary penetration leads to a rise in the moisture content as the liquid front moves. Therefore, a correlation existed between the liquid front and moisture content during the first measurement points (Fig. 11b). During capillary penetration, no swelling took place which can be seen in Fig. 11a, where the liquid front advanced while swelling is constant. Therefore, it was assumed that the penetration process is unaffected by swelling. In other types of paper, swelling can become important. This should subsequently be taken into

account for the penetration process, which is done in some theoretical models (Chang & Kim, 2020). From Section 3.2.3, we know that the liquid front will trap air within the liquid system. The orange circle in 12a shows the development of an air bubble.

During phase II, the swelling phase, the paper swells from its initial thickness h_1 to a new thickness h_2 , see Fig. 12b. It was found in Section 3.2.2 that a decrease in fiber density was responsible for a further increase in the moisture content. This relation between swelling and moisture content can be seen in Fig. 11c where a linear relationship exists between moisture content and swelling during phase II (yellow arrow). In this stage, air is surrounded by water and becomes completely trapped (orange circle).

In the final phase, the moisture content increased without a change in swelling or front position (Fig. 11b,c). In Section 3.2.3 it was shown that the release of trapped air is responsible for the increase in moisture content. Fig. 12c shows how during this phase, the paper thickness stays constant and the air bubbles get smaller (orange circle). It was also shown that the air escaped via the surface of the paper sample. A similar observation was made by Waldner et al. where the presence of air bubbles in the paper after capillary penetration, and their subsequent release, was observed in ultrasonic testing of liquid penetration (Waldner & Hirn, 2020).

5. Conclusions

In this paper, the liquid penetration mechanism inside a cellulose fiber network was investigated with UFI NMR. We were able to simultaneously measure the liquid distribution, swelling and trapped air within a paper sample. The liquid penetration process could be split into 3 different phases: 1) liquid front penetration, 2) swelling and 3) the release of entrapped air. During the first phase, capillary forces drove water into the system. This phase lasted for only 65 ms and resulted in a water saturation of 40 v/v%. During the penetration, around 15 v/v% of air is entrapped within the system. Following capillary uptake, the paper entered a 30 s swelling phase. During this phase, the paper swelled around 45 % which led to a further increase in the water density towards 55 v/v% attributed to a reduction in the fiber content. During the final phase, the air that was entrapped during capillary uptake was slowly replaced by water. This phase lasted around 3 h. The study confirmed the hypothesis that, within hydrophilic paper, liquid penetration is governed by capillary uptake and that it can be decoupled from swelling.

The UFI method employed in this study allowed to simultaneously

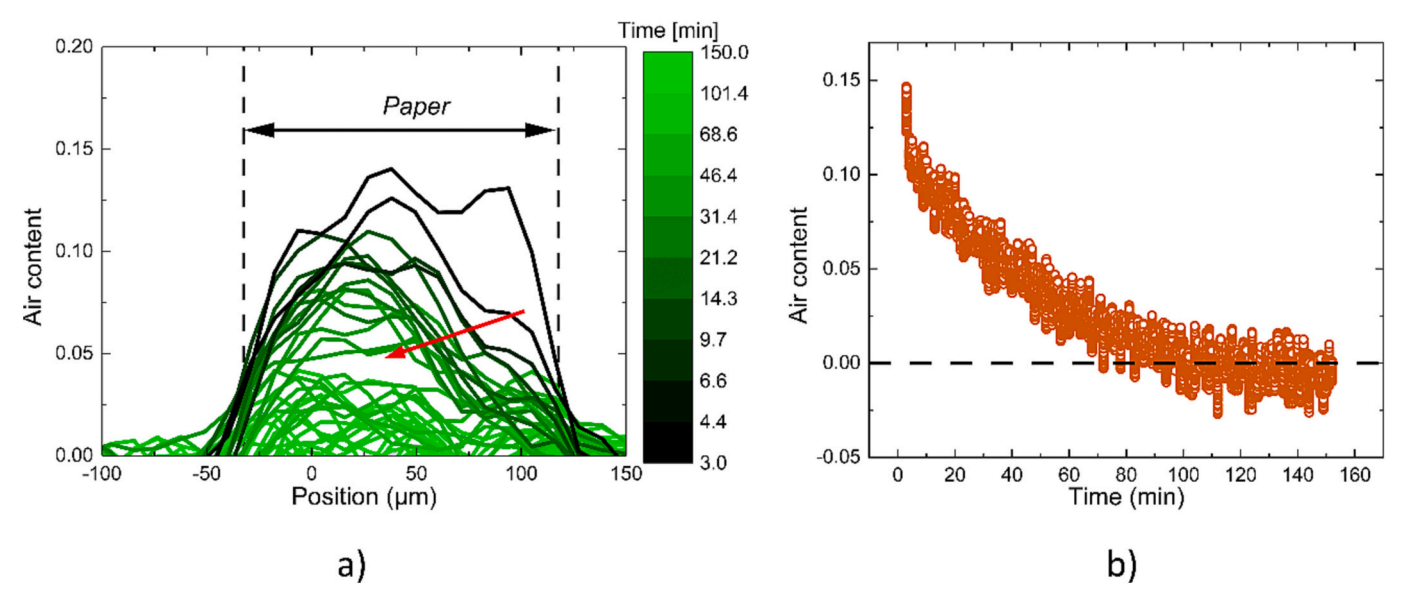


Fig. 10. a) Air fraction profiles in paper during phase III. The position of the paper sheet at the start of phase III is marked with dashed lines. Red arrow is used to mark the movement of the arrow within the paper through time. b) Air fraction integrated over the whole paper samples as a function of time.

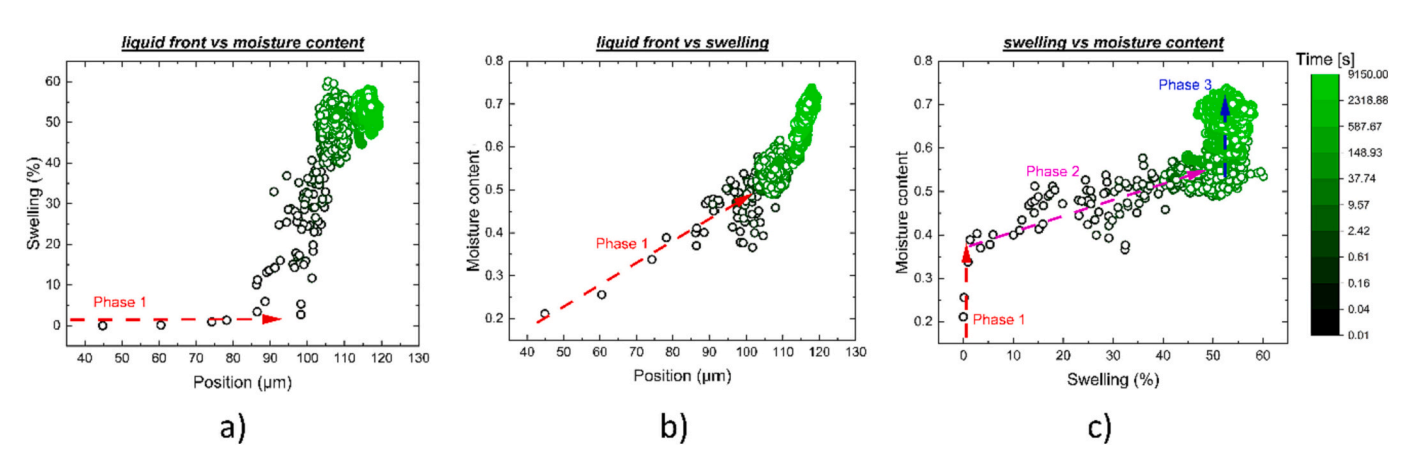


Fig. 11. a) Swelling as a function of liquid front. b) Moisture content as a function of liquid front. c) Moisture content as a function of swelling.

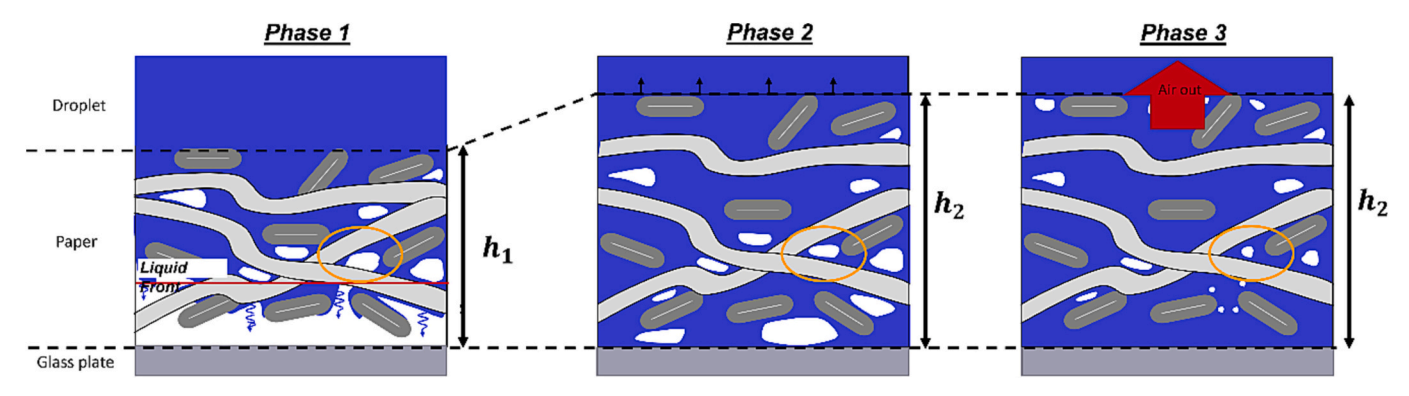


Fig. 12. Schematic representation of the liquid uptake in paper. Shown are the three different phases: capillary liquid uptake, swelling and the release of trapped air. The orange circle follows the development of an air bubble within the paper sample.

study the liquid distribution, swelling and trapped air with a spatial- and temporal resolution of 14.5 μm -18 μm and 10 ms respectively. This allowed to study the liquid uptake in cellulose fiber networks in much more spatial- and temporal detail than most existing methods. However, further improvements on temporal resolution and signal-to-noise ratio could increase the impact of this technique. The strength of the method

is that it becomes possible to quantify the concentration of all three phases, solid, liquid and air within the network at high temporal resolution. We hence believe that the proposed method should also be useful to study liquid penetration, or water diffusion, into other porous cellulosic materials like foams, membranes, nonwovens, textiles and films.

CRediT authorship contribution statement

R.J.K. Nicasy: Conceptualization, Data curation, Formal analysis, Investigation, Methodology, Visualization, Writing – original draft. C. Waldner: Conceptualization, Data curation, Formal analysis, Investigation, Writing – original draft. S.J.F. Erich: Conceptualization, Funding acquisition, Supervision, Writing – review & editing. O.C.G. Adan: Conceptualization, Funding acquisition, Supervision, Writing – review & editing. U. Hirn: Conceptualization, Investigation, Writing – review & editing. H.P. Huinink: Conceptualization, Investigation, Funding acquisition, Project administration, Supervision, Writing – review & editing.

Declaration of competing interest

The authors declare that they have no known competing financial

interests or personal relationships that could have appeared to influence the work reported in this paper.

Data availability

Data will be made available on request.

Acknowledgements

This publication is part of the project PQP (Print Quality and Particles) (Project No. 17099) of the research collaboration program High Tech Systemen en Materialen (HTSM) 2018 TTW, which was (partly) financed by the Dutch Research Council (NWO). The researchers would also like to thank H. Dalderop (TU/e) and M. Kurvers (TU/e) for helping to build the experimental setup. Last, we would like to thank Covestro and Canon Production Printing for their support.

Appendix A. Integrated moisture content

In this appendix it is shown how the total moisture content between -118 μ m and 150 μ m can provide information about the fiber content within the paper. The situation is schematically given in Fig. A1.

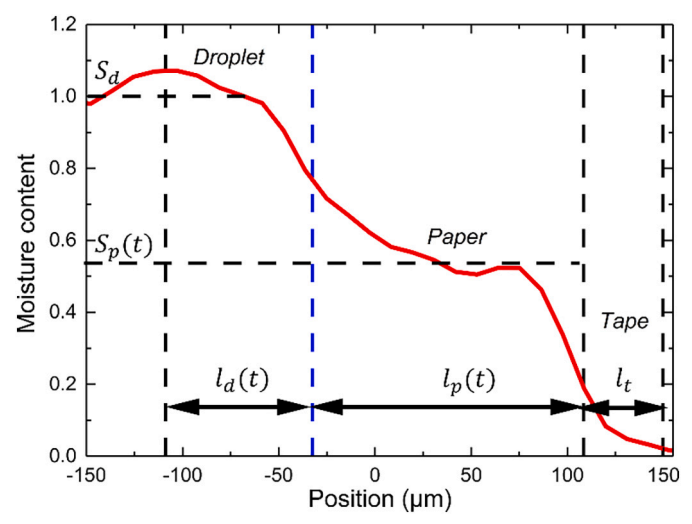


Fig. A1. Moisture profile measured during stage two. The integrated area between $-118 \ \mu m$ and 150 μm is marked by black dashed lines, together with the corresponding droplet $(l_d(t))$ and paper area $(l_p(t))$. The moisture content within the droplet (S_d) and paper $(S_p(t))$ are also marked.

The moisture content is integrated between $-118~\mu m$ and $150~\mu m$, see Fig. A1 and is given by,

$$S(t) = \int_{-1.9}^{1.50} S(x, t) dx \tag{A1}$$

This area can be split up in three parts, the droplet area $l_a(t)$, the paper domain $l_p(t)$ and the tape l_t . For simplicity, and because the signal in the tape is almost zero, the tape area will be neglected here. Both the droplet and paper position depend on the paper thickness and are therefore time dependent. When using both regions, the equation becomes:

$$S(t) = \int_{-118}^{150 - l_{\rm p}(t) - l_{\rm t}} S_{\rm d}(x, t) dx + \int_{150 - l_{\rm p}(t) - l_{\rm t}}^{150 - l_{\rm t}} S_{\rm p}(x, t) dx$$
(A2)

Because the droplet consists of only liquid, $S_d(x,t) = 1$, which results in:

$$S(t) = (268 - l_{p}(t) - l_{t}) + \int_{150 - l_{p}(t) - l_{t}}^{150 - l_{t}} S_{p}(x, t) dx$$
(A3)

It is also known that the signal within the paper can be related to the air and fiber content by: $S_p = 1 - \rho_{\text{fiber}}(x, t) - \rho_{\text{air}}(x, t)$. Using this relation, we end up with:

$$S(t) = \left(268 - l_{p}(t) - l_{t}\right) + \int_{150 - l_{n}(t) - l_{t}}^{150 - l_{t}} 1 dx - \int_{150 - l_{n}(t) - l_{t}}^{150 - l_{t}} a\rho_{\text{fiber}}(x, t) dx - \int_{150 - l_{n}(t) - l_{t}}^{150 - l_{t}} b\rho_{\text{air}}(x, t) dx$$
(A4)

When assuming that the air is incompressible, we know that $\int_{150-l_p(t)-l_i}^{150-l_i} a \rho_{\text{fiber}}(x,t) \mathrm{d}x = \text{constant}$. When implementing this condition and doing some calculations, we end up with:

$$S(t) = 268 - C_{\text{air}} - \int_{150 - l_o(t) - l_o}^{150 - l_t} a\rho_{\text{fiber}}(x, t) dx = \text{constant}$$
(A5)

Because we know from Fig. 8 b that S(t) = 0.53 during phase II, therefore we know that,

$$\int_{150-l_{\rm n}(t)-l_{\rm t}}^{150-l_{\rm n}} a\rho_{\rm fiber}(x,t) dx = -0.53 + 268 - C_{\rm air} = {\rm constant}$$
(A6)

Therefore, we can conclude that if the integrated signal S(t) is constant, the total fiber content within the integrated area is also constant.

Appendix B. T_1 and T_2 relaxation times of a Clariscan solution in paper during phase III (1-300 min.)

To prove that the T_1 and T_2 relaxation time are not responsible for the measured signal changes during phase III of the absorption process, an extended NMR pulse experiment was performed. The experimental procedure is shown in Fig. B1. Because the focus lies on the later uptake process, 5 drops are directly added, followed by closing the sample holder. After the paper comes in contact with the water the NMR will start to measure the UFI signal, the T_2 relaxation time with an OW sequence ($t_e = 50 \, \mu s$, $t_r = 0.1 \, s$) and the T_1 time with a saturation recovery sequence. Because the T_1 time of a Clariscan solution is low enough to ensure fast recovery of the spins. All measurements can be performed within 5 min.

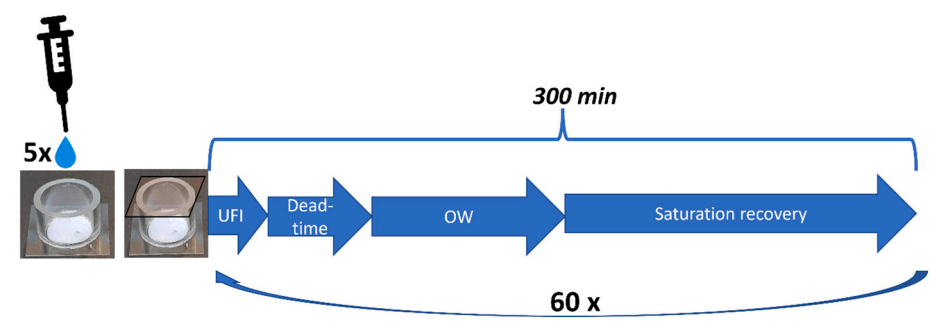


Fig. B1. Experiment type II, to measure the UFI-signal intensity, T_2 relaxation time and T_1 relaxation time during phase III for a Clariscan-water solution within a paper sample. The measurements together take approximately 5 min to perform. This sequence is then repeated 60 times which results in a total measurement time of 300 min.

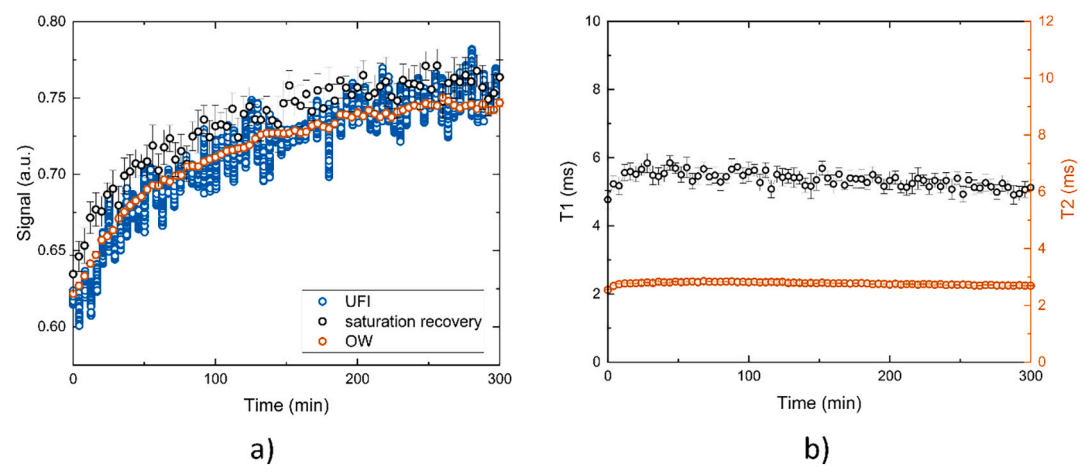


Fig. B2. a) Signal intensities during the uptake of a Clariscan-water solution in a paper sheet as measured by UFI (blue), OW-measurement (orange) and saturation recovery (black). b) T_1 and T_2 relaxation times during the uptake of a Clariscan-water solution in a paper sheet. (For interpretation of the references to colour in this figure legend, the reader is referred to the web version of this article.)

Fig. B2 shows the signal intensity, measured with all three pulse sequences, UFI (blue), OW-measurement (orange) and saturation recovery (black). The signal intensities from the OW- and saturation recovery sequence do not depend on the relaxation times and are comparable to the signal intensity measured with UFI. Therefore, the change in signal intensity measured by UFI cannot be linked to a change in T_2 or T_1 time. Besides the signal intensities, Fig. B2b shows the T_1 and T_2 times measured during phase III which show that both relaxations times stay constant over the course of 300 min, again showing that, the signal change should be attributed to an increase in ρ , the water content.

References

Alava, M., & Niskanen, K. (2006). "The physics of paper." ON PROGRESS IN PHYSICS Rep. Progress in Physics, 69, 669–723. https://doi.org/10.1088/0034-4885/69/3/R03

Baukh, V., Huinink, H. P., Adan, O. C. G., Erich, S. J. F., & van der L.G.J. Ven.. (2012). Predicting water transport in multilayer coatings. *Polymer*, 53(15), 3304–3312. https://doi.org/10.1016/J.POLYMER.2012.05.043 Baukh, V., Huinink, H. P., Adan, O. C. G., Erich, S. J. F., & van der Ven, L. G. J. (2011). Water-polymer interaction during water uptake. *Macromolecules*, 44(12), 4863–4871. https://doi.org/10.1021/MA102889U

Berli, C., See Claudio, L. A., Berli, E. E., Urteaga, R., & Berli, C. L. A. (2015). Rational design of capillary-driven flows for paper-based microfluidics. *Lab on a Chip*, 15(10), 2173–2180. https://doi.org/10.1039/C4LC01487A

Bloembergen, N., Purcell, E. M., & Pound, R. V. (1948). Relaxation effects in nuclear magnetic resonance absorption. *Physical Review*, 73(7), 679. https://doi.org/ 10.1103/PhysRev.73.679

Blumich, B. (2000). NMR imaging of materials. Oxford University Press.

- Bolden, J., Corder, Z., Higdon, C., & Miller, C. (2015). Measuring surface tension using the
- Bosanquet, C. M. (1923). On the flow of liquid into capillary tubes. The London, Edinburgh, and Dublin Philosophical Magazine and Journal of Science, 45(267), 525–531. https://doi.org/10.1080/14786442308634144
- Botková, M., Šutý, Š., Jablonský, M., Kucerkova, L., & Vrška, M. (2013). Monitoring of Kraft pulps swelling in water. Cellulose Chemistry and Technology, 47(2), 95–102.
- Chang, S., & Kim, W. (2020). Dynamics of water imbibition through paper with swelling. Journal of Fluid Mechanics, 892, A39. https://doi.org/10.1017/JFM.2020.219
- Chang, S., Seo, J., Hong, S., Lee, D.-G., & Kim, W. (2018). Dynamics of liquid imbibition through paper with intra-fibre pores. *Journal of Fluid Mechanics*, 845, 36–50. https://doi.org/10.1017/jfm.2018.235
- Cui, C., Lin, G., Dai, L., Ji, N., Yang, Q., Shi, R., ... Sun, Q. (2023). Hydrophobic biopolymer-based films: Strategies, properties, and food applications. *Food Engineering Reviews*, 15(2), 360–379. https://doi.org/10.1007/S12393-023-09342-6, 2023 15:2.
- De Azevedo, E. N., Alme, L. R., Engelsberg, M., Fossum, J. O., & Dommersnes, P. (2008). Fluid imbibition in paper fibers: Precursor front. *Physical Review E Statistical, Nonlinear, and Soft Matter Physics, 78*(6), Article 066317. https://doi.org/10.1103/PHYSREVE.78.066317/FIGURES/5/MEDIUM
- Falzone, S., & Keating, K. (2016). A laboratory study to determine the effect of pore size, surface Relaxivity, and saturation on NMR T2 relaxation measurements. Near Surface Geophysics, 14(1), 57–69. https://doi.org/10.3997/1873-0604.2016001
- Ferreira, E. S., Drummond, J., Veiga, A. T. V., Sibellas, A., Brown, S., Cranston, E. D., & Mark Martinez, D. (2023). Mapping absorbency in cellulosic fibres with iron tracers. *Carbohydrate Polymers*, 311, Article 120785. https://doi.org/10.1016/j.carbpol.2023.120785
- Gezici-Koç, Ö., Erich, S. J. F., Huinink, H. P., van der Ven, L. G. J., & Adan, O. C. G. (2017). Bound and free water distribution in wood during water uptake and drying as measured by 1D magnetic resonance imaging. *Cellulose*, 24(2), 535–553. https:// doi.org/10.1007/S10570-016-1173-X/TABLES/4
- Glover, P. M., Aptaker, P. S., Bowler, J. R., Ciampi, E., & McDonald, P. J. (1999). A novel high-gradient permanent magnet for the profiling of planar films and coatings. *Journal of Magnetic Resonance*, 139(1), 90–97. https://doi.org/10.1006/ imre.1999.1772
- Gong, M. M., & Sinton, D. (2017). Turning the page: Advancing paper-based microfluidics for broad diagnostic application. *Chemical Reviews*, 117(12), 8447–8480. https://doi.org/10.1021/ACS.CHEMREV.7B00024
- Han, Y., Manolach, S. O., Denes, F., & Rowell, R. M. (2011). Cold plasma treatment on starch foam reinforced with wood fiber for its surface hydrophobicity. *Carbohydrate Polymers*, 86, 1031–1037. https://doi.org/10.1016/j.carbpol.2011.05.056
- Heard, P. J., Preston, J. S., Parsons, D. J., Cox, J., & Allen, G. C. (2004). Visualisation of the distribution of ink components in printed coated paper using focused ion beam techniques. Colloids and Surfaces A: Physicochemical and Engineering Aspects, 244 (1–3), 67–71. https://doi.org/10.1016/J.COLSURFA.2004.05.012
- Hürlimann, M. D. (2001). Diffusion and relaxation effects in general stray field NMR experiments. *Journal of Magnetic Resonance (San Diego, Calif.: 1997)*, 148(2), 367–378. https://doi.org/10.1006/JMRE.2000.2263
- Jablonsky, M., Botková, M., Šutý, Š., Šmatko, L., & Jozef, Š. (2014). Accelerated ageing of newsprint paper: Changes in swelling ability, WRV and electrokinetic properties of fibres. Fibres & Textiles in Eastern Europe, 22(2), 108–113.
- Jacques, V., Dumas, S., Sun, W.-C., Troughton, J. S., Greenfield, M. T., & Caravan, P. (2010). High relaxivity MRI contrast agents part 2: Optimization of inner-and second-sphere relaxivity. *Investigative Radiology*, 45(10), 613–624. https://doi.org/10.1097/RIJ.0b013e3181ee6a49
- Krainer, S., Smit, C., & Hirn, U. (2019). The effect of viscosity and surface tension on inkjet printed picoliter dots. RSC Advances, 9(54), 31708–31719. https://doi.org/ 10.1039/c9rs04093b
- Kuijpers, C. J., Huinink, H. P., Tomozeiu, N., Erich, S. J. F., & Adan, O. C. G. (2017). Sorption of water-glycerol mixtures in porous Al2O3 studied with NMR imaging. Chemical Engineering Science, 173, 218–229. https://doi.org/10.1016/j. ces.2017.07.035
- Kuijpers, C. J., van Stiphout, T. A. P., Huinink, H. P., Tomozeiu, N., Erich, S. J. F., & Adan, O. C. G. (2018). Quantitative measurements of capillary absorption in thin porous media by the automatic scanning absorptometer. *Chemical Engineering Science*, 178, 70–81. https://doi.org/10.1016/j.ces.2017.12.024
- Kumar, S., Mukherjee, A., & Dutta, J. (2022). Biopolymer-based food packaging: Innovations and technology applications. In Biopolymer-based food packaging: Innovations and technology applications (pp. 1–490). https://doi.org/10.1002/ 9781119702313
- Kunam, K., Praveen, D. R., Akhila, K., & Gaikwad, K. K. (2022). Bio-based materials for barrier coatings on paper packaging. *Biomass Conversion and Biorefinery*.. https://doi. org/10.1007/s13399-022-03241-2
- Lamminmäki, T. T., Kettle, J. P., & Gane, P. A. C. (2011). Absorption and adsorption of dye-based inkjet inks by coating layer components and the implications for print quality. *Colloids and Surfaces A: Physicochemical and Engineering Aspects*, 380(1–3), 79–88. https://doi.org/10.1016/J.COLSURFA.2011.02.015
- Letková, E., Letko, M., & Vrška, M. (2011). Influence of recycling and temperature on the swelling ability of paper. *Chemical Papers*, 65(6), 822–828. https://doi.org/10.2478/ S11696-011-0089-Z
- Lundberg, A., Örtegren, J., Alfthan, E., & Ström, G. (2011). Paper-ink interactions: Microscale droplet absorption into paper for inkjet printing. Nordic Pulp & Paper Research Journal, 26(1), 142–150. https://doi.org/10.3183/NPPRJ-2011-26-01-P142-150

- Markley, J. L., Horsley, W. J., & Klein, M. P. (1971). Spin-lattice relaxation measurements in slowly relaxing complex spectra. *The Journal of Chemical Physics*, 55(7), 3169–3177. https://doi.org/10.1063/1.1676626
- Masoodi, R., & Pillai, K. M. (2010). Darcy's law-based model for wicking in paper-like swelling porous media. AICHE Journal, 56(9), 2257–2267. https://doi.org/10.1002/ AIC.12163
- Merbach, A., Helm, L., & Toth, É. (2013). The chemistry of contrast agents in medical magnetic resonance imaging: Second edition. Second Edition: The Chemistry of Contrast Agents in Medical Magnetic Resonance Imaging.
- Müller-Petke, M., Dlugosch, R., Lehmann-Horn, J., & Ronczka, M. (2015). Nuclear magnetic resonance average pore-size estimations outside the fast-diffusion regime. *Geophysics*, 80(3), D195–D206. https://doi.org/10.1190/GEO2014-0167.1
- Murali, V., Venditti, G., Zeegers, J. C. H., & Darhuber, A. A. (2021). Inkjet deposition of lines onto thin moving porous media - experiments and simulations. *International Journal of Heat and Mass Transfer*, 176, Article 121466. https://doi.org/10.1016/J. LJHEATMASSTRANSFER, 2021.121466
- Nicasy, R., Huinink, H. P., Erich, S. J. F., & Adan, O. C. G. (2021). High-speed NMR imaging of capillary action in thin nontransparent porous media. *Physical Review E*, 104(4), L043101. https://doi.org/10.1103/PhysRevE.104.L043101
- Nicasy, R. J. K., Huinink, H. P., Erich, S. J. F., Adan, O. C. G., & Tomozeiu, N. (2023). Ultra fast imaging NMR method for measuring fast transport processes in thin porous media. Magnetic Resonance Imaging, 103, 61–74. https://doi.org/10.1016/j. mrj 2023 06 009
- Nicasy, R., Huinink, H., Erich, B., & Adan, O. (2022). NMR profiling of reaction and transport in thin layers: A review. *Polymers*, 14(4), 798. https://doi.org/10.3390/ POLYM14040798, 2022, Vol. 14, Page 798.
- Ostroff, E. D., & Waugh, J. S. (1966). Multiple spin echoes and spin locking in solids. Physical Review Letters, 16(24), 1097–1098. https://doi.org/10.1103/ PhysRevLett.16.1097
- Parada, M., Vontobel, P., Rossi, R. M., Derome, D., & Carmeliet, J. (2017). Dynamic wicking process in textiles. *Transport in Porous Media*, 119, 611–632. https://doi.org/ 10.1007/s11242-017-0901-5
- Patari, S., & Mahapatra, P. S. (2020). Liquid wicking in a paper strip: An experimental and numerical study. https://doi.org/10.1021/acsomega.0c02407
- Perrin, J. C., Waldner, C., Bossu, J., Chatterjee, A., & Hirn, U. (2022). Real time monitoring of the through thickness moisture profile of thin sheets using NMR. Chemical Engineering Science, 251. https://doi.org/10.1016/J.CES.2022.117464
- Ridgway, C. J., Gane, P. A. C., & Schoelkopf, J. (2002). Effect of capillary element aspect ratio on the dynamic imbibition within porous networks. *Journal of Colloid and Interface Science*, 252, 373–382. https://doi.org/10.1006/jcis.2002.8468
- Rohadi, T. N. T., Ridzuan, M. J. M., Abdu, M. S., Majid, E. M. C., Norasni, M. J., & Marsi, N. (2021). Swelling behaviors of composite film with alternating fibre reinforcement and aqueous media. *Journal of Physics: Conference Series*, 2051(1). https://doi.org/10.1088/1742-6596/2051/1/012024
- Rostom, L., Caré, S., & | Denis Courtier-Murias.. (2021). Analysis of water content in wood material through 1D and 2D 1 H NMR relaxometry: Application to the determination of the dry mass of wood. *Magnetic Resonance in Chemistry*, 59(6), 614–627. https://doi.org/10.1002/mrc.5125
- Salam, A., Venditti, R. A., Pawlak, J. J., & El-Tahlawy, K. (2011). Crosslinked hemicellulose citrate-chitosan aerogel foams. Carbohydrate Polymers, 84, 1221–1229. https://doi.org/10.1016/j.carbpol.2011.01.008
- Salem, K. S., Naithani, V., Jameel, H., Lucia, L., & Pal, L. (2022). A systematic examination of the dynamics of water-cellulose interactions on capillary forceinduced fiber collapse. *Carbohydrate Polymers*, 295, Article 119856. https://doi.org/ 10.1016/J.CARPOL. 2022.119856
- Salminen, P. (1988). Studies of water transport in paper during short contact times. Ph.D. Thesis. Turku, Finland: Abo Akademi University.
- Samyn, P. (2013). Wetting and hydrophobic modification of cellulose surfaces for paper applications. *Journal of Materials Science*, 48(19), 6455–6498. https://doi.org/ 10.1007/S10853-013-7519-Y
- Schoelkopf, J., Ridgway, C. J., Gane, P. A. C., Matthews, G. P., & Spielmann, D. C. (2000). Measurement and network modeling of liquid permeation into compacted mineral blocks. *Journal of Colloid and Interface Science*, 227, 119–131. https://doi.org/ 10.1006/jcis.2000.6885
- Tang, K. P. M., Wu, Y. S., Chau, K. H., Kan, C. W., & Fan, J. T. (2015). Characterizing the transplanar and in-plane water transport of textiles with gravimetric and image analysis technique: Spontaneous uptake water transport tester. https://doi.org/10.1038/ srep09689
- Tang, X. Z., Kumar, P., Alavi, S., & Sandeep, K. P. (2012). Recent advances in biopolymers and biopolymer-based nanocomposites for food packaging materials. 52 (5), 426–442. https://doi.org/10.1080/10408398.2010.500508
- Topgaard, D., & Söderman, O. (2001). Diffusion of water absorbed in cellulose fibers studied with 1H-NMR. *Langmuir*, 17(9), 2694–2702. https://doi.org/10.1021/ LA000982L/ASSET/IMAGES/LARGE/LA000982LF00016.JPEG
- Venditti, G., Murali, V., & Darhuber, A. A. (2022). Inkjet printing of surfactant solutions onto thin moving porous media. Colloids and Surfaces A: Physicochemical and Engineering Aspects, 634, Article 127832. https://doi.org/10.1016/J. COLSURFA.2021.127832
- Waldner, C., & Hirn, U. (2020). Ultrasonic liquid penetration measurement in thin sheets—Physical mechanisms and interpretation. *Materials*, 13(12), 2754. https://doi.org/10.3390/MA13122754, 2020, Vol. 13, Page 2754.
- Waldner, C., & Hirn, U. (2023). Modeling liquid penetration into porous materials based on substrate and liquid surface energies. *Journal of Colloid and Interface Science*, 640, 445–455. https://doi.org/10.1016/J.JCIS.2023.02.116
- Waldner, C., Mayrhofer, A., & Hirn, U. (2022). Measuring liquid penetration in thin, porous sheets with ultrasound and drop absorption Scope and limitations. *Colloids*

- and Surfaces A: Physicochemical and Engineering Aspects, 650, Article 129551. https://doi.org/10.1016/J.COLSURFA.2022.129551
- Wijburg, M. G., Wang, S., & Darhuber, A. A. (2023). Transport and evaporation of aqueous co-solvent solutions in thin porous media. *Colloids and Surfaces A: Physicochemical and Engineering Aspects*, 656, Article 130268. https://doi.org/ 10.1016/J.COLSURFA.2022.130268
- Xu, J., Liu, F., Wang, T., Goff, H. D., & Zhong, F. (2020). Fabrication of films with tailored properties by regulating the swelling of collagen fiber through ph adjustment. https://doi. org/10.1016/j.foodbyd.2020.106016
- org/10.1016/j.foodhyd.2020.106016

 Zhang, H., Tong Zhao, Y., Chen, X. H., Yanfang, X., Guangbiao, X., Wang, F., ... Shen, H. (2022). A sustainable nanocellulose-based superabsorbent from kapok fiber with advanced oil absorption and recyclability. *Carbohydrate Polymers, 278*, Article 118948. https://doi.org/10.1016/j.carbpol.2021.118948